

LithoHoD: A Litho Simulator-Powered Framework for IC Layout Hotspot Detection

Hao-Chiang Shao, *Member, IEEE*, Guan-Yu Chen, Yu-Hsien Lin, Chia-Wen Lin, *Fellow, IEEE*, Shao-Yun Fang, *Member, IEEE*, Pin-Yian Tsai, and Yan-Hsiu Liu

Abstract—Recent advances in VLSI fabrication technology have led to die shrinkage and increased layout density, creating an urgent demand for advanced hotspot detection techniques. However, by taking an object detection network as the backbone, recent learning-based hotspot detectors learn to recognize only the problematic layout patterns in the training data. This fact makes these hotspot detectors difficult to generalize to real-world scenarios. We propose a novel lithography simulator-powered hotspot detection framework to overcome this difficulty. Our framework integrates a lithography simulator with an object detection backbone, merging the extracted latent features from both the simulator and the object detector via well-designed cross-attention blocks. Consequently, the proposed framework can be used to detect potential hotspot regions based on i) the variation of possible circuit shape deformation estimated by the lithography simulator, and ii) the problematic layout patterns already known. To this end, we utilize RetinaNet with a feature pyramid network as the object detection backbone and leverage LithoNet as the lithography simulator. Extensive experiments demonstrate that our proposed simulator-guided hotspot detection framework outperforms previous state-of-the-art methods on real-world data.

Index Terms—Design for manufacturability, convolutional neural networks, hotspot detection, lithography simulation, defect detection.

I. INTRODUCTION

With the rapid advances in the semiconductor industry, process nodes are transitioning from the tens to the single digits,

Manuscript received on 10 April 2024; revised 2 August 2024; accepted 15 September 2024. Date of publication Month Date, 2024; date of current version Month Date, 2024. This work was supported in part by the National Council of Science and Technology, Taiwan, under Grants NSTC 112-2634-F-002-005 and NSTC 112-2221-E-005-080, and in part by United Microelectronics Corporation. The associate editor coordinating the review of this manuscript and approving it for publication was Dr. Laleh Behjat. (Corresponding Author: Chia-Wen Lin)

Hao-Chiang Shao is with the Institute of Data Science and Information Computing, National Chung Hsing University, Taichung 402202, Taiwan. (e-mail: shao.haochiang@gmail.com)

Guan-Yu Chen and Yu-Hsien Lin are with the Department of Electrical Engineering, National Tsing Hua University, Hsinchu 300044, Taiwan.

Chia-Wen Lin is with the Department of Electrical Engineering and the Institute of Communications Engineering, National Tsing Hua University, Hsinchu 300044, Taiwan. (e-mail: cwlin@ee.nthu.edu.tw)

Shao-Yun Fang is with the Department of Electrical Engineering, National Taiwan University of Science and Technology, Taipei 106335, Taiwan. (e-mail: syfang@mail.ntust.edu.tw)

Pin-Yian Tsai is with the Product Engineering Department, United Microelectronics Corporation, Hsinchu 300094, Taiwan. (e-mail: pin_yian_tsai@umc.com)

Yan-Hsiu Liu is with the Development of Smart Manufacturing, United Microelectronics Corporation, Hsinchu 300094, Taiwan. (e-mail: Cecil_liu@umc.com)

Color versions of one or more of the figures in this paper are available online at <http://ieeexplore.ieee.org>.

resulting in increased transistor density and making identifying defect patterns on wafers more challenging. This poses an issue for designers when they attempt to correct their layout design and mitigate defects. To this end, hotspot detection in integrated circuit (IC) fabrication is a crucial process that entails identifying and analyzing specific areas within a chip design susceptible to potential manufacturing or operational challenges. These “hotspots” denote regions where particular conditions or patterns might give rise to defects, compromised performance, or other undesirable outcomes throughout the fabrication process or in the operation of the final IC.

The significance of hotspot detection lies in its pivotal role during the design and verification phases of IC development, ensuring the creation of high-quality and dependable semiconductor devices. This intricate task employs specialized tools and algorithms to scrutinize the layouts and designs of ICs, searching for patterns or configurations that could lead to issues such as timing violations, excessive power consumption, or challenges associated with fabrication processes like lithography. Early identification of hotspots in the design phase empowers engineers and manufacturers to implement corrective measures promptly. These measures may involve optimizing the design, adjusting manufacturing processes, or introducing enhancements to alleviate potential problems. This proactive approach enhances the overall yield, reliability, and performance of ICs, ultimately creating more efficient and resilient electronic devices.

Traditionally, designers employ a scanning electron microscope (SEM) to scrutinize post-process images of a wafer to identify defects. However, with denser designs comes the need for more high-resolution SEM images to meet defect detection requirements, leading to substantial time and labor costs. Although pattern-matching approaches can quickly detect hotspot patterns on a layout design, they are still not robust against novel design patterns.

Recently, several learning-based methods have been proposed to address this problem by adopting convolutional neural network (CNN) based object detection models [1], [2], [3], [4], [5], [6], [7]. By regarding a layout hotspot region as an object, the hotspot detection problem can be recast as an object detection issue, where the solver aims to identify different objects, *i.e.*, hotspots, in an input image along with their classification probabilities and bounding-box regions. This consideration has led to the recent design trend in this type of approach. For example, Chen *et al.* [4] devised a hotspot detector based on Faster-RCNN [8]. Their model employs an inception-based feature extractor and a clip proposal network

to generate region proposals, improving recall performance, reducing false alarms, and increasing computation speed.

However, by using a general object detector as the backbone, conventional learning-based hotspot detectors only learn to recognize problematic layout patterns similar to the hotspot ground-truths in the training data. This makes conventional hotspot detectors struggle to generalize to real-world applications, where different layouts may result in similar hotspot circuit appearances due to fabrication process variations. To address this issue, we propose a **Litho** (lithography) simulator-powered **Hotspot Detector (LithoHoD)** for real-world layout hotspot detection tasks.

Fig. 1 illustrates the differences between the design concepts of LithoHoD and conventional hotspot detectors. Traditional methods rely solely on object detectors to identify regional structures of layout patterns prone to causing hotspots. In contrast, LithoHoD integrates a lithography simulator, using its predicted deformation map to improve feature embedding for the object detection network, thus enhancing hotspot identification. Specifically, LithoHoD learns the triune relationship among fabrication imperfections (*i.e.*, the predicted deformation maps), layout patterns, and hotspot ground truths during the training process. LithoHoD integrates a learning-based lithography simulator with an object detection network by fusing their feature tensors via well-designed cross-model feature fusion modules. This design enables LithoHoD to recognize different local design patterns that may lead to similar defect appearances after fabrication, thereby improving detection accuracy. As a result, by learning the triune relationship between i) circuit layouts, ii) circuit fabrication outcomes, and iii) hotspot ground truths, our method can detect potential hotspot regions based on the possible variations in circuit shape distortions estimated by the lithography simulator and the problematic layout patterns already learned.

The main contribution of this paper is twofold. First, we propose a simulator-powered framework for layout hotspot detection. With the aid of a pretrained lithography simulator, the proposed framework is able to detect potential hotspot regions instead of identifying a hotspot pattern already seen. Second, we propose a cross-attention block that guides the fusion of the feature tensor extracted by the lithography simulator with that extracted by common object detection networks. Our extensive experiments demonstrate the effectiveness of the proposed framework.

II. RELATED WORK

In this work, we propose formulating IC layout hotspot detection as a supervised learning-based visual object detection problem based on the layout shape features, involving the interactions between the neighboring layout designs and the lithography-induced shape deformation. This section reviews the most relevant methods in learning-based hotspot detection, object detection, and lithography simulation.

A. Learning-based Hotspot Detection Methods

Since Yu *et al.* [9] proposed a pioneering machine learning-based hotspot detection method in 2013, learning-based approaches have already demonstrated the capability in layout

hotspot detection tasks. For example, Matsunawa *et al.* [10] presented a hotspot detection framework utilizing an Adaboost classifier and a simplified feature extraction scheme. Later, Yang *et al.* develop a CNN-based hotspot detection method based on features derived by a traditional static image compression scheme [3]. In Yang *et al.*'s approach, a layout is first transformed into frequency domain features patch-wisely by using a discrete cosine transform followed by a zig-zag scan to form a feature tensor; then, the resulting feature tensor is fed into a LeNet-styled neural network to derive the detection result. Additionally, Chen *et al.* [4] proposed a hotspot detection method based on Faster-RCNN, employing an inception module as its feature extraction backbone. Despite achieving good detection accuracy, the above three methods incur high computational time costs due to the design of the network framework. Hence, Gai *et al.* [5] proposed a computationally efficient lightweight network model to reduce computation. However, this method is specialized as a binary hotspot detector and is thus unable to recognize different hotspot categories. As a result, this method needs to be re-trained to adapt to hotspot patterns of different types.

Additionally, the data security issue in layout hotspot detection problems has been addressed recently. Specifically, Lin *et al.* [11] employed heterogeneous federated learning, facilitating the adaptation of the global model to local data heterogeneity while preserving the privacy of local data and preventing the leakage of layout designs. This is particularly crucial for advanced process nodes in today's competitive landscape as companies strive to safeguard their designs from external exposure.

B. Object detection networks

Object detection has been among the most widely utilized computer vision techniques since anchor-based deep object detection networks (*e.g.*, R-CNN [12]) were introduced. Deep object detection networks are generally categorized into two types, namely one-stage and two-stage detectors, based on whether a pre-generated region proposal is employed in the object detection process. Typically, two-stage detectors achieve higher accuracy, but often lead to longer execution times due to repeated computations. The representative two-stage detectors belong to the R-CNN family [12], [13], [8]. Using a fixed number of predefined anchors as candidate regions for analysis, R-CNN [12] extracts deep features from these candidates and classifies them via a support vector machine. Fast R-CNN [13] further improves computation efficiency by converting an input image into a base feature tensor at the outset. It then crops regional features from the feature tensor based on predefined candidate regions for subsequent classification and bounding box regression tasks. Subsequently, Faster R-CNN [8] then introduces a region proposal network (RPN) for suggesting region proposals at runtime, improving recognition performance and saving computation costs by performing computations on only those regions identified by the RPN.

In contrast, one-stage detectors perform region localization and object classification concurrently, making them faster but

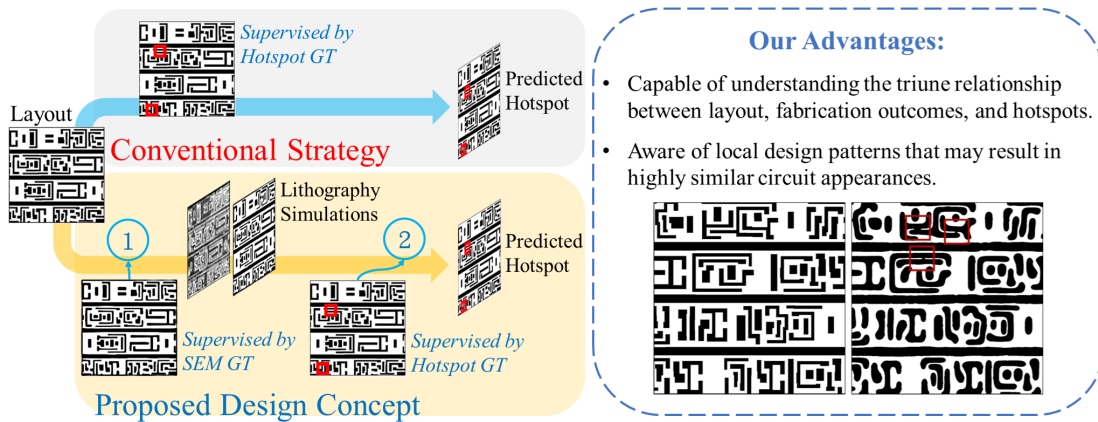


Fig. 1. Differences in the design concepts between traditional hotspot detectors and ours. While a traditional hotspot detector is trained as a naive hotspot pattern recognizer with the supervision of hotspot ground-truths, our design aims to learn the triune relationship among layout, fabrication outcomes, and hotspots. This design enables **LithoHoD** to recognize local design patterns that may lead to highly similar circuit appearances of hotspots. As a result, **LithoHoD** functions as a versatile hotspot detector capable of identifying not only layout defect patterns but also considering circuit shape deformations due to a fabrication process to pinpoint potential hotspots. Hotspot regions in this figure are indicated with red boxes.

less accurate than two-stage detectors. Representative one-stage object detectors include the YOLO family [14], [15], [16], [17], SSD [18], and RetinaNet [19]. Particularly, RetinaNet addresses the data imbalance problem, caused by the uneven distribution between foreground and background objects, using focal loss. It also utilizes the Feature Pyramid Network (FPN) [20] to recognize objects across different sizes and observation scales. These improvements enable RetinaNet to run as fast as one-stage detectors while maintaining accuracy comparable to two-stage detectors. Therefore, building upon RetinaNet, we devise our layout hotspot detection model.

C. Lithography Simulators

Traditionally, two approaches have been employed to obtain a post-process aerial image of an IC layout. One involves a real fabrication procedure to acquire a SEM (scanning electron microscope) image of a product IC. In contrast, the other utilizes lithography simulators, such as ICWB (IC WorkBench) by Synopsys. However, both of these conventional methods are expensive and time-consuming. Consequently, several neural network-based lithography simulation models were proposed to address this challenge [21], [22], [23], [7], [24]. In particular, LithoNet [24], a data-driven learning-based lithography simulator, can predict the circuit shape deformation due to the lithography and etching processes involved in IC fabrication with varying fabrication parameters. LithoNet learns the circuit shape correspondence from paired layout and SEM images to estimate a deformation map through a multi-scale generator, as illustrated in the upper branch of Fig. 2. This deformation map and the latent features derived by LithoNet capture crucial information such as circuit shapes and deformation variances. Hence, LithoNet is further employed to construct a novelty-based active-learning framework for best updating a pre-trained lithography simulator [25]. Building upon the capabilities of LithoNet and leveraging its deformation map as a guidance feature, we propose a model-guided lithography hotspot detection method in this paper, namely **LithoHoD**.

III. LITHOGRAPHY SIMULATOR-POWERED HOTSPOT DETECTOR

A. Overview

We devise a lithography simulator-assisted framework for layout hotspot detection. The proposed framework, as depicted in Fig. 2, comprises four components: i) a pretrained lithography simulator, ii) an object detection network, iii) a channel-wise attention (C-Attn) module within the object detector backbone, and iv) our devised cross-model feature fusion (CMF) modules, each comprising two self-attention modules and one cross-attention module. C-Attn aims to enhance the coarsest features extracted from the layout pattern by the object detector. Additionally, the CMF module is designed to fuse tensors of different domains and dimensions: the deformation features generated by the lithography simulator and the pattern features generated by the object detector backbone. The self-attention mechanism in the CMF module enhances the representability of its input tensor by exploring the dependency between two different spatial positions within the tensor, whereas the cross-attention mechanism transfers the simulator's prediction of circuit shape deformation to the object detection network, enabling the recognition of potential hotspot areas. This design enables the proposed framework to detect hotspots based on the learnable relationship between layout patterns, lithography distortions, and defect patterns in the training dataset.

LithoHoD requires a more comprehensive training dataset than previous hotspot detection methods. This dataset includes i) layout patterns, ii) hotspot ground truths, and iii) SEM images of product ICs, where the third one is not used in the traditional methods. The training process for LithoHoD consists of two stages: pre-training and main training. In the pre-training stage, the lithography simulator (LithoNet) is trained using pairs of layout patterns and their corresponding SEM images. During the main training stage, the pretrained LithoNet, serving as the upper branch of LithoHoD, predicts circuit shape deformation maps (*i.e.*, local shape deformation features) caused by an imperfect fabrication process. These

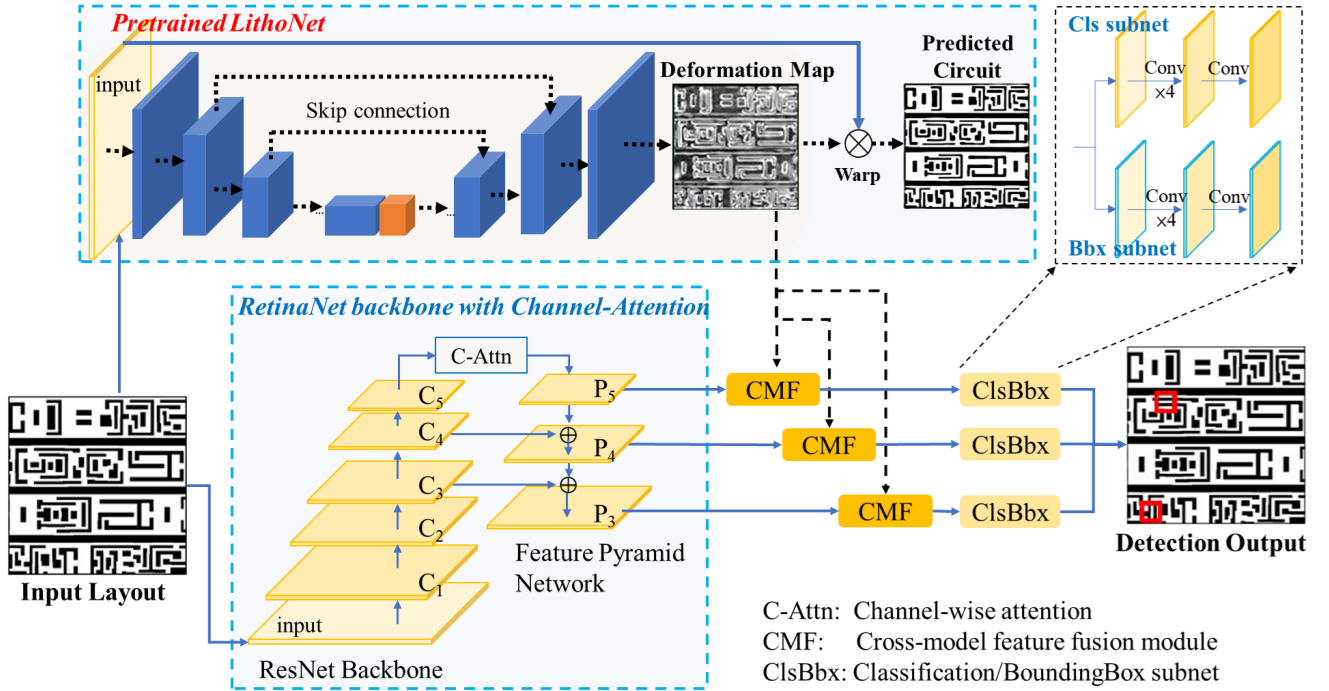


Fig. 2. Framework of the proposed LithoHoD. This framework comprises two primary functional components: a pretrained lithography simulator (LithoNet) and a trainable object detector (Channel-attention-enhanced RetinaNet). This design includes a channel-wise attention (C-Attn) module and three cross-model feature fusion (CMF) modules. The C-Attn module enhances the representability of the feature tensor used in the RetinaNet backbone. In contrast, the CMF modules facilitate the integration of the shape-deformation feature f_{de} with detection features $f_{py,l}$ in three distinct observation scales extracted by the feature pyramid network (FPN). Here, the tensor C_l corresponds to the output of the l -th convolution stage, and its dimension is 2^l times lower than the original input. P_l is the tensor derived by the pyramid structure with the same spatial dimension as C_l . Note that, i) the FPN in RetinaNet omits the P_2 and P_1 layers in its design, ii) our implementation removes the P_6 and P_7 layers of the original FPN used in RetinaNet, and iii) the architecture of the detector module **ClsBbx**, consisting of a classification subnet and a box regression subnet, is detailed in Table II.

deformation features are then fused with the layout shape features extracted by the object detector (RetinaNet) in the lower branch, which is trained on pairs of layout patterns and hotspot ground truths. This fusion, achieved through the self- and cross-attention mechanisms of the Cross-Model-Feature (CMF) module, enables more accurate hotspot detection by leveraging the complementary features provided by the lithography simulator.

In the following subsections, we will elaborate on each component of our framework design.

B. LithoNet: Assessing lithography distortion

Hotspot detection aims to identify and analyze chip design areas prone to potential manufacturing or operational issues, *e.g.*, distortions caused by the lithographic process. To identify potential hotspots, including those caused by lithography gaps and those sensitive to the lithographic process [26], we utilize a pretrained data-driven lithography simulator LithoNet that we proposed in [24] in the proposed hotspot detection framework to assess lithography distortions. This design allows our detector to consider factors such as lithography distortions and fabrication parameters, which have not yet been explored in existing CNN-based hotspot detection approaches. Specifically, LithoNet can generate a lithography prediction \mathcal{J}' and a shape deformation map \mathcal{M} for an input layout clip by learning the shape correspondence between the training layout patterns \mathcal{S} and their lithography ground-truth \mathcal{J} (*i.e.*, the

corresponding SEM image). Thus, the predicted deformation map $\mathcal{M} : \mathbf{R}^2 \rightarrow \mathbf{R}^2$ records the pixel-wise displacement vectors between individual pixels (x_S, y_S) on a layout image \mathcal{S} and the pixel position $(x_{\mathcal{J}}, y_{\mathcal{J}})$ on the associated SEM image \mathcal{J} . Consequently, the warping operator, illustrated in the upper half of Fig. 2, transforms an input layout shape into its corresponding fabricated circuit shape based on the predicted displacement vectors from the predicted deformation map \mathcal{M} . As a result, the deformation map, which records the displacement vectors of individual pixels, provides features that represent pixel-wise lithography distortions. This deformation map \mathcal{M} is then considered as a deformation feature f_{de} that can potentially guide the layout hotspot detection process.

However, the deformation map predicted by LithoNet only consists of pixel-wise displacement vectors, which is insufficient to capture the interactions between the layout contours within their local neighborhood. Therefore, we enhance the deformation map by using a self-attention module to assess the inter-pixel dependencies. As reported in [25], the self-attention module enhances a feature tensor by assessing how the feature of the i -th element of the tensor contributes to that of the j -th element. This enhancement process facilitates the learning of local interactions between shapes within a neighborhood and results in the deformation feature f_{de} , representing the attention the pretrained lithography simulator provides. The deformation feature f_{de} can then be utilized to assist the layout hotspot detection process through a cross-attention module.

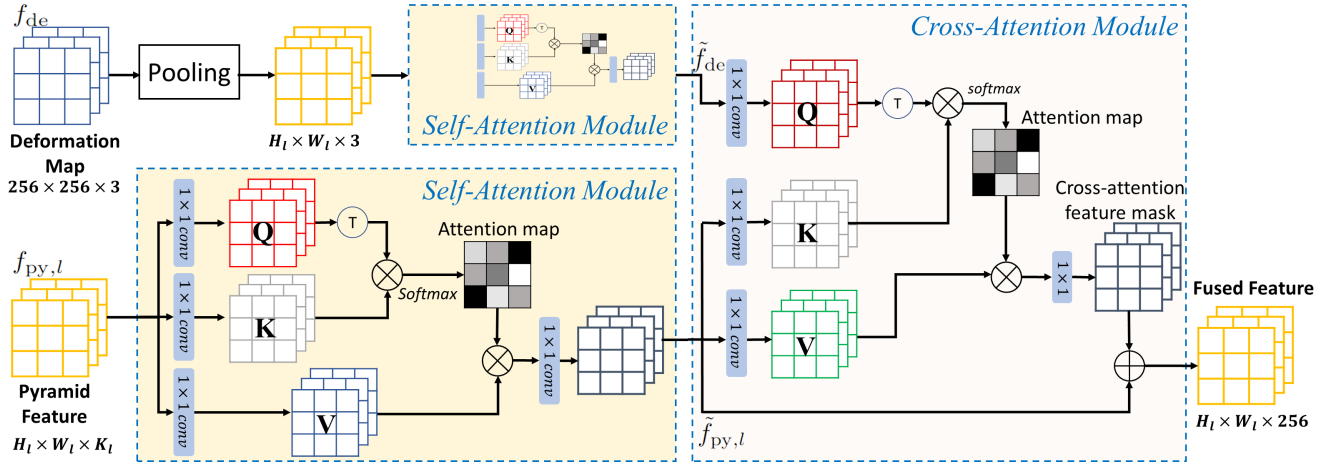


Fig. 3. Proposed Cross-Model Feature Fusion (CMF) module. This module is designed to generate a fused model-guided feature for layout hotspot detection. To this end, CMF comprises two self-attention modules and one cross-attention module. Specifically, one self-attention module enhances the shape-deformation feature (*i.e.*, the deformation map f_{de}) generated by the pre-trained lithography simulator. Besides, the other self-attention module processes the pattern feature (*i.e.*, the pyramid feature $f_{py,l}$ for object detection) derived from the feature pyramid network of the channel-attention-enhanced RetinaNet backbone. The two enhanced and adapted feature tensors are then fed into the cross-attention module for cross-model feature fusion. Note that the two self-attention modules share the same architecture, and the dimension of each feature tensor used in the CMF module is shown in Table I.

Note that the pre-trained LithoNet learns to predict lithography distortions from training data pairs consisting of i) a layout pattern and ii) the product IC's SEM images of the given layout, using the loss terms described in [24]. LithoNet is essentially a CNN aiming to predict the fabricated circuit shape of an input layout. In other words, the pre-trained LithoNet is knowledgeable about the circuit shape distortion caused by a fabrication process. Additionally, the labeled hotspot ground truths required for LithoHoD's main training stage will not be altered by the pretrained LithoNet.

C. Object Detection Backbone

The backbone of the proposed hotspot detection framework is a modified RetinaNet, which is enhanced with a channel-wise attention module. RetinaNet [19] is a widely adopted object detection system known for its high detection accuracy and low computational cost. The feature extraction backbone of RetinaNet is built upon ResNet [27] and FPN (feature pyramid network) [20]. In the original RetinaNet design, the ResNet backbone converts an input image into multi-stage feature tensors. Subsequently, FPN utilizes these multi-stage feature tensors as inputs to generate feature tensors of different observation scales for the subsequent object recognition and classification stage. This design enables RetinaNet to learn multi-resolution features that are robust to the changes in the target object size.

In our design, we make several modifications to RetinaNet. First, we added the channel-wise attention (CA) module, used in the CBAM (Convolutional Block Attention Module) [28], to the connection between the deepest feature tensor outputted by ResNet and the coarsest-level input of FPN. This channel-wise attention module allows our network to learn the importance of individual channels in the high-level feature tensor, which is particularly helpful for characterizing the shape properties of layout patterns composed exclusively of polygons, as opposed to real-world objects, for subsequent hotspot detection [28].

Second, to efficiently merge feature tensors of layout patterns, we modified the network architecture of RetinaNet [19] and FPN [20] by removing the P_6 and P_7 layers from their original designs¹. Instead, we employed a shallower architecture comprising only P_3 , P_4 , and P_5 layers². In other words, we construct a feature pyramid with levels P_3 through P_5 , where P_l has a resolution of 2^l times lower than the original input image, where l represents the pyramid level. This modification not only reduces the network parameters but also prevents the use of feature tensors that correspond to a representation that is too coarse to capture the local interaction of layout contours. Hence, this modification can avoid possible overfitting caused by binary and polygonal layout patterns. Third, we incorporate an additional self-attention module (within the cross-model feature fusion module, which will be introduced later) to enhance the multi-resolution feature tensors generated by FPN. This self-attention module improves the multi-resolution features by focusing on local interactions between layout contours within a neighborhood.

D. Cross-Model Feature Fusion (CMF) Module

Inspired by the self-attention module proposed in [29] and its extension in the application to layout novelty detection [25], we devise a Cross-Model Feature Fusion (CMF) module. As shown in Fig. 3, this module consists of two self-attention blocks and a meticulously designed cross-attention block, which enables the integration of the lithography simulator with the object detector. This integration facilitates a lithography simulator-guided hotspot detection process.

One main issue in merging the deformation map f_{de} extracted by the lithography simulator and the l -th level pyramid feature $f_{py,l}$ (*i.e.*, the pattern feature shown in Fig. 3) obtained

¹Please refer to the third-party implementation of RetinaNet: <https://github.com/yhenon/pytorch-retinanet/blob/master/retinanet/model.py>

²The FPN of RetinaNet does not include the P_2 and P_1 layers in its design.

from the modified RetinaNet for object detection lies in aligning these two feature tensors. To this end, we first reduce the spatial dimension of deformation map f_{de} using global average pooling³ to match that of $f_{py,l}$. Then, the spatially aligned deformation map and the pyramid feature individually pass through two independent self-attention modules to align their channel dimensions, allowing them to be effectively fused using the cross-attention block we devise. Fig. 3 illustrates the block diagrams of our cross-model feature fusion (CMF) module that consists of two self-attention blocks and one cross-attention block in our implementation. Considering that each layer of the pyramid features is individually fed into an object detection subnetwork of RetinaNet, three CMF modules aim to independently integrate the deformation features into the P_3 , P_4 , and P_5 layers of the pyramid features, as illustrated in Fig. 2. Notice that we use \tilde{f}_{de} and $\tilde{f}_{py,l}$ to denote the tensors enhanced and aligned by the self-attention modules, respectively.

Cross-Attention Block. We adopt the architecture of the self-attention module from SA-LithoNet [25] and repurpose it into our cross-attention block. While the self-attention block enhances the representability of its input feature tensor by providing it with an attention map on a wider neighborhood based on the input itself, the cross-attention block improves its target tensor based on an attention map recording the contribution the i -th element of the guiding tensor brings to the j -th element of the target tensor. As a result, the guiding tensor in our cross-attention block is enhanced with a wide-range representative feature for capturing the fabrication-induced shape deformation of a circuit. The proposed cross-attention block takes the enhanced deformation feature \tilde{f}_{de} as the input of the *query* (**Q**) branch and the enhanced pyramid detection feature $\tilde{f}_{py,l}$ as the inputs of the *key* (**K**) and *value* (**V**) branches. The cross-attention computation can be formulated in the following matrix form:

$$\mathbf{Q} = \mathbf{W}_q^T \tilde{\mathbf{f}}_{de}, \quad \mathbf{K} = \mathbf{W}_k^T \tilde{\mathbf{f}}_{py,l}, \quad \mathbf{V} = \mathbf{W}_v^T \tilde{\mathbf{f}}_{py,l}, \quad (1)$$

where $\tilde{\mathbf{f}}_{de}$ and $\tilde{\mathbf{f}}_{py,l}$ represent the deformation and pyramid feature tensors enhanced by the self-attention modules, respectively, and \mathbf{W}_q^T , \mathbf{W}_k^T , and \mathbf{W}_v^T denote 1×1 convolution kernels. Via tensor reshaping, the dimensions of $\tilde{\mathbf{f}}_{de}$ and $\tilde{\mathbf{f}}_{py,l}$ become $C_1 \times (H \cdot W)$ and $C_2 \times (H \cdot W)$, respectively, where H and W are the height and the width of the tensor. Meanwhile, the dimensions of \mathbf{W}_q^T , \mathbf{W}_k^T , and \mathbf{W}_v^T are $C_1 \times C$, $C_2 \times C$, and $C_2 \times C$, respectively. Notably, in our implementation, $C = 32$, $C_1 = 3$, and $C_2 = 256$.

As a result, the attention map of the cross-attention block

³Deformation map \mathcal{M} records the pixel-wise displacement vectors of a $W \times H$ input layout image. Downsampling (average-pooling) the deformation map to fit the different spatial dimensions of the feature tensors (P_3 – P_5) from different layers of the FPN does not lead to information loss. Specifically, the deformation map is resized to $h_i \times w_i$ via average pooling to guide the hotspot detector layer with a $h_i \times w_i$ feature tensor P_i by feature fusion. As a result, the hotspot detection process is conducted in a multi-resolution fashion, where the resized deformation features are fused with feature tensors P_3 – P_5 of the coarse-to-fine detection branches in parallel at different observation scales. This process thus does not lead to information loss.

TABLE I
DIMENSION OF EACH FEATURE TENSOR USED IN THE PROPOSED
CROSS-MODEL FEATURE FUSION (CMF) MODULE

Tensors	Self-Attention Blocks		Cross-Attention Block
	f_{de}	$f_{py,l}$	
Input	$256 \times 256 \times 3$	$H_l \times W_l \times K_l$	$f_{de}: H_l \times W_l \times 3$
After pooling	$H_l \times W_l \times 3$	--	$f_{py,l}: H_l \times W_l \times 256$
Q	$H_l \times W_l \times 3$	$H_l \times W_l \times 16$	$H_l \times W_l \times 32$
K	$H_l \times W_l \times 3$	$H_l \times W_l \times 16$	$H_l \times W_l \times 32$
V	$H_l \times W_l \times 3$	$H_l \times W_l \times 16$	$H_l \times W_l \times 32$
Attention map	$H_l W_l \times H_l W_l$	$H_l W_l \times H_l W_l$	$H_l W_l \times H_l W_l$
Output	$H_l \times W_l \times 3$	$H_l \times W_l \times 256$	$H_l \times W_l \times 256$

* $W_5=H_5=16$, $K_5=2048$; $W_4=H_4=32$, $K_4=1024$; and, $W_3=H_3=64$, $K_3=512$.

in the Fig. 3 can be derived by

$$\beta_{j,i} = \frac{e^{s_{ij}}}{\sum_{i=1}^{HW} \sum_{j=1}^{HW} e^{s_{ij}}}, \quad (2)$$

where $s_{ij} = \mathbf{q}_i^T \mathbf{k}_j$; \mathbf{q}_i and \mathbf{k}_j are $C \times 1$ sub-tensors, and $\beta_{j,i}$ represents the normalized attention (*i.e.*, the dependency) in the j -th location contributed by the i -th region.

Consequently, the output cross-attention feature mask $\mathbf{M} = (\mathbf{m}_1, \mathbf{m}_2, \dots, \mathbf{m}_j, \dots, \mathbf{m}_{HW})$ is a $C_2 \times (W \cdot H)$ tensor with \mathbf{m}_j defined as

$$\mathbf{m}_j = \mathbf{W}_m^T \sum_{i=1}^{HW} \beta_{j,i} \mathbf{v}_i, \quad (3)$$

where \mathbf{v}_i denotes the i -th $C_2 \times 1$ sub-tensor of the $C_2 \times (W \cdot H)$ value map, and \mathbf{W}_m^T denotes a 1×1 convolution kernel with a dimension of $C \times C_2$.

Consequently, the final feature tensor $\mathbf{f}_{XA}(\mathbf{x})$ enhanced by this cross-attention module becomes

$$\mathbf{f}_{XA} = \xi \mathbf{M} + \tilde{\mathbf{f}}_{py,l}, \quad (4)$$

where ξ is a learnable parameter, initialized as 1. Note that the dimension of \mathbf{f}_{XA} is identical to the cross-attention feature mask \mathbf{M} , *i.e.*, $C_2 \times (W \cdot H)$, in the matrix representation, and \mathbf{f}_{XA} is a $H \times W \times C_2$ tensor in our implementation.

This cross-attention block can learn the spatial dependency between the two input feature tensors and thus extract a tensor more representative than its input for hotspot detection. We take this cross-attention detection feature \mathbf{f}_{XA} in (4) as the input for the subsequent detector module depicted in Subsection III-E.

Self-Attention Block. Our self-attention Block is structurally a simplified version of the cross-attention block described above. Concisely speaking, taking the self-attention block for the deformation map \mathbf{f}_{de} provided by the lithography simulator for example, its *query*, *key* and *value* maps are defined as $\mathbf{Q}_{self} = \mathbf{W}_{Qs}^T \mathbf{f}_{de}$, $\mathbf{K}_{self} = \mathbf{W}_{Ks}^T \mathbf{f}_{de}$, and $\mathbf{V}_{self} = \mathbf{W}_{Vs}^T \mathbf{f}_{de}$, respectively. The attention map of the self-attention module is defined in the same way as in (2). As a result, the self-attention block outputs a tensor, whose each $C_s \times 1 \times 1$ sub-sensor is defined similarly to (3). Table I summarizes the dimensions of individual feature tensors used in the proposed cross-attention block.

TABLE II
ARCHITECTURES OF BOUNDING-BOX REGRESSION SUBMODULE AND CLASSIFIER SUBMODULE

Submodule	Functional Layers		
	Conv2D+ReLU	Final Conv.	Final Activation
BBox-Regression	×4	×1	–
Classification	×4	×1	Sigmoid

E. Detector Module

The detector module is responsible for inferring the object category and locating the object bounding box from its input feature tensor at the end of the object detection network. A detector module usually consists of two sub-networks: a classification subnet and a box regression subnet. This subsection explains the detector configuration of the proposed LithoHoD. The architectures of our classification and box regression subnets are shown in Table II.

Classification Subnet. The classification subnet aims to predict the category probability of a target object, along with a hotspot area. Given that our proposed simulator-guided hotspot detector is adopted from a RetinaNet [19] backbone, we highlight the key settings below.

First, because the proposed LithoHoD adopts a five-level feature pyramid network instead of the original seven-level architecture, it only utilizes three different sizes of anchors: 32×32 for P_3 , 64×64 for P_4 , and 128×128 for P_5 , respectively. Second, the hyper-parameter **SCALES** is reconfigured to be $[0.25, 0.5, 1.0, 2.0]$. This hyper-parameter controls the usage of either enlarged or shrunk anchors, enabling the hotspot detector to identify hotspot regions of variable sizes. Third, the hyper-parameter **ASPECT_RATIO** in the anchor configurations remains unchanged as $[0.5, 1.0, 2.0]$. This hyper-parameter controls the possible changes in the aspect ratio of an anchor for object detection. Last, building upon the previous points, we use 12 anchors of varying sizes in each classification subnet, achieved by combining four scales and three aspect ratios. Finally, the classification submodule is implemented as *Conv2d-ReLU-Conv2d-ReLU-Conv2d-ReLU-Conv2d-ReLU-Conv2d-Sigmoid*, where the final *Sigmoid* layer generates a probability vector for classification. All convolution kernels are of size 3×3 .

Box Regression Subnet. The box regression subnet works with the classification subnet. It generates a 4×1 vector to describe the four vertices of the bounding box of each detected area. The box regression subnet is architecturally identical to the classification subnet, except it lacks the final activation layer. Specifically, the architecture of the box regression subnet is *Conv2d-ReLU-Conv2d-ReLU-Conv2d-ReLU-Conv2d-ReLU-Conv2d*. Note that the box regression subnet and the classification subnet do not share any parameters.

F. Loss Function

The total loss function used to train our proposed LithoHoD is composed of three loss terms: the α -balanced focal loss [19], the bounding box regression loss, and the distance-

IoU loss [30]. The α -balanced focal loss, used to train a classification subnet, is defined as

$$\mathcal{L}_{\text{FL}} = \mathbb{E}(\ell_{\text{FL}}), \quad (5)$$

where $\mathbb{E}(\cdot)$ denotes the expectation function, and ℓ_{FL} is defined as follows:

$$\ell_{\text{FL}}(p_t) = -\alpha_t(1 - p_t)^\gamma \log(p_t), \quad (6)$$

where p_t is the probability that the training sample x_t belongs to category y , and α and γ are empirically set to be 0.25 and 2, respectively. Notice that p_t is obtained by

$$p_t = \begin{cases} p & , \text{ if } x_t \in y \\ 1 - p & , \text{ otherwise} \end{cases} . \quad (7)$$

Moreover, the bounding box regression loss is defined as the Huber loss (*aka* smooth- L_1 loss). That is,

$$\mathcal{L}_r = \mathbb{E}(\ell_r), \quad (8)$$

where

$$\ell_r = \begin{cases} 0.5 \cdot (\mathbf{v} - \mathbf{v}_{\text{GT}})^2 & , \text{ if } |\mathbf{v} - \mathbf{v}_{\text{GT}}| < 1 \\ |\mathbf{v} - \mathbf{v}_{\text{GT}}| - 0.5 & , \text{ otherwise} \end{cases} . \quad (9)$$

In this equation, \mathbf{v} and \mathbf{v}_{GT} denote the predicted 4×1 vector specifying the bounding box and the ground-truth vector, respectively.

Finally, the the distance-IoU loss [30] is defined as

$$\mathcal{L}_{\text{DIoU}} = \mathbb{E}(\ell_{\text{DIoU}}), \quad (10)$$

and

$$\ell_{\text{DIoU}} = 1 - \text{IoU} + \frac{|\mathbf{b} - \mathbf{b}_{\text{GT}}|^2}{c_{\text{diag}}}. \quad (11)$$

Here, $|\mathbf{b} - \mathbf{b}_{\text{GT}}|$ denotes the Euclidean distance between the central point of the predicted bounding box and that of the ground-truth bounding box, c_{diag} is the diagonal length of the smallest enclosing box covering the two boxes, and IoU is the *Intersection-over-Union* value of the two boxes defined as

$$\text{IoU} = \frac{\text{Area of Overlap region of two Boxes}}{\text{Area of Union of two Boxes}}. \quad (12)$$

Consequently, the total loss is defined as

$$\mathcal{L}_{\text{total}} = \mathcal{L}_r + \mathcal{L}_{\text{FL}} + \lambda \mathcal{L}_{\text{DIoU}}, \quad (13)$$

with $\lambda = 0.02$.

IV. EXPERIMENTAL RESULTS

A. Datasets

As detailed in Table III, two datasets are utilized to verify the effectiveness of the proposed framework: 1) the **ICCAD16** open dataset [31], and 2) the **UMC20K** dataset, a private dataset provided by UMC (United Microelectronics Corporation). **ICCAD16** encompasses four layout designs, namely, Case-1, Case-2, Case-3, and Case-4. In each layout of **ICCAD16**, the left-half part is used for generating training samples via random clipping, whereas the right-half part is used to generate testing samples through non-overlapping clipping. Each clipped sample is of dimension 256×256 , corresponding to a physical size of $2.56\mu\text{m} \times 2.56\mu\text{m}$. **ICCAD16** focuses

TABLE III

DATASET DETAILS ABOUT (1) **ICCAD16** AND (2) **UMC20K**. WHILE EACH CASE IN **ICCAD16** CONTAINS ONLY ONE SOURCE LAYOUT, **UMC20K** IS CONSTRUCTED USING 1,300 PROCESS TEST KEYS

Dataset	# of Source Layouts	Layout size (μm^2)		# of Hotspots		# of Clips		Clips size (μm^2)	Image Dimension (pixels)
		Train	Test	Train	Test	Train	Test		
ICCAD16-2	1	6.95×3.75	6.95×3.75	40	39	1,000	8	2.56×2.56	256×256
ICCAD16-3	1	12.91×10.07	12.91×10.07	1,388	1,433	1,000	33	2.56×2.56	256×256
ICCAD16-4	1	79.95×42.13	79.95×42.13	90	72	1,000	55	2.56×2.56	256×256
UMC20K	1,300	200×200	200×200	81,984	8,011	20,120	2,887	2×2	512×512

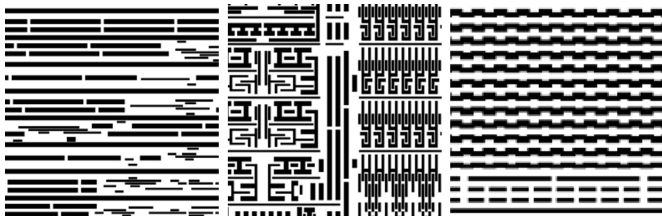


Fig. 4. Examples from ICCAD16 dataset. Left: Case-2. Middle: Case-3. Right: Case-4. Each case consists of a layout sample, with its left-half used for training data and the right-half for testing data. The dimensions of the half-size for Case-2, Case-3, and Case-4 are respectively $6.95\mu\text{m} \times 3.75\mu\text{m}$, $12.91\mu\text{m} \times 10.07\mu\text{m}$, and $79.95\mu\text{m} \times 42.13\mu\text{m}$.

solely on EPE (Edge Placement Error), Bridging, and Necking defects. Since Case-1 is defect-free, it is excluded from our experiments. We follow the data generation rules described in [3], [4].

UMC20K comprises 20,120 training samples and 2,887 testing samples. These clips are collected from UMC’s real-world process test keys, as illustrated in Fig. 5. Due to various functional considerations during IC circuit design, different chip regions often have different circuit appearances. For example, regions focusing on audio signal processing have appearances close to analog circuit designs, whereas regions for video signal processing exhibit digital circuit appearances. Therefore, **UMC20K** is divided into six subsets, from digital to analog circuit appearances, based on UMC’s production line experience. Each sample in **UMC20K** is a 512×512 clip, corresponding to a physical size of $2\mu\text{m} \times 2\mu\text{m}$, taken from either a fabrication layout or a simulation layout. Additionally, each sample contains multiple hotspot areas. Since **UMC20K** is a real-world dataset that is richer and more diverse than common open datasets like **ICCAD16**, we utilize it to verify the generalizability of the proposed LithoHoD and to conduct comparisons with previous state-of-the-art methods, including BBL-HoD [3], R-HSD [4], and FCN-HoD [5].

B. Experiment Configurations

To implement the proposed LithoHoD, we employ ResNet-34 as the feature extraction backbone used in RetinaNet. Because we utilize our LithoNet [24], [25] as the lithography simulator to guide LithoHoD, all input layout clips are resized to 512×512 to fit the receptive field of the pretrained LithoNet. The ground-truth hotspot area size of **ICCAD16** is 69×69 , consistent with the settings used in [3], [4]. For **UMC20K**, the ground-truth hotspot area size is 100×100 . The LithoNet model is pretrained on a dataset of paired samples to capture

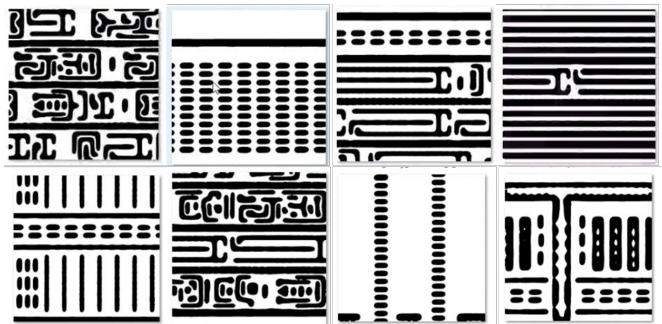


Fig. 5. Example clips of **UMC20K** dataset, presented through their lithographic simulation results. The **UMC20K** dataset comprises 23,007 design clips representing digital and analog circuits, categorized into six subsets.

the deformations of circuit shapes from each layout to its corresponding SEM (Scanning Electron Microscope) image, as detailed in [24]. For the subsequent experiments, we utilize this pretrained LithoNet model to implement LithoHoD and evaluate its performance on the **ICCAD16** and **UMC20K** datasets.

We also set an IoU threshold for the training process. Specifically, a detected bounding box is classified as positive (*i.e.*, a hotspot) if the IoU score between it and the corresponding ground-truth is greater than 0.5. In contrast, those with an IoU score less than 0.3 are classified as negative. If no positive region can be found in an input layout clip, our detector considers the one with the largest IoU value greater than 0.3 as positive; otherwise, the clip is regarded as defect-free.

For the experiments on **ICCAD16**, each of the three images (case-2, case-3, and case-4) in **ICCAD16** is partitioned into two halves: one half for generating randomly cropped training patches and the other for generating testing patches. Specifically, the experiments shown in Table IV are conducted using the left half for training and the right half for testing. In contrast, Table V(A) shows the results where the right half is used for training and the left half for testing. In the experiment shown in Table V(B), we vertically split each image into three horizontal strips and use the middle strip for training and the bottom strip for testing since the top strip contains no hotspot. Moreover, for the experiments of R-HSD [4] on **ICCAD16**, by following the official setting, a detected hotspot area is considered a true positive if the distance between the predicted bounding box center and the ground-truth bounding box center is no more than $\frac{1}{3} \times 69 = 23$. This results in an approximate IoU threshold value of 0.42, which is more lenient than the threshold of 0.5 used for FCN-HoD and LithoHoD.

TABLE IV

PERFORMANCE COMPARISON OF LITHOHOD WITH VARIOUS FEATURE EXTRACTION BACKBONES AND THREE SOTA METHODS ON **ICCAD-16**. HERE, THE BEST RESULTS ARE HIGHLIGHTED IN BOLD, AND THE SECOND-BEST RESULTS ARE UNDERLINED. BESIDES, THE VALUES IN PARENTHESES ARE THE DATA REPORTED IN THE PAPERS OF THE SOTA METHODS, AND THE OTHERS ARE FROM OUR EXPERIMENTAL RESULTS.

Datasets	Method	Recall	#FA	#FN	Time (s)
ICCAD16 Case-2	BBL-HoD [3]	(0.778)	(48)	(9)	(60)
	R-HSD [4]	0.304	291	48	1.65
		(0.957)	(15)	(2)	(2.30)
	FCN-HoD [5]	0.058	21	65	22.3
		(0.974)	(92)	(1)	(0.20)
	Ours (Res18)	0.986	65	1	0.53
Ours (Res34)	<u>0.971</u>	<u>55</u>	<u>2</u>	<u>0.55</u>	
Ours (Res50)	0.942	63	3	0.58	
ICCAD16 Case-3	BBL-HoD [3]	(0.912)	(263)	(127)	(265)
	R-HSD [4]	0.983	119	23	4.51
		(0.947)	(78)	(76)	(10.8)
	FCN-HoD [5]	0.002	1	1776	76.04
		(0.978)	(102)	(32)	(1.00)
	Ours (Res18)	0.964	179	51	2.22
Ours (Res34)	0.974	78	38	<u>2.28</u>	
Ours (Res50)	<u>0.980</u>	149	<u>30</u>	2.34	
ICCAD16 Case-4	BBL-HoD [3]	(1.000)	(511)	(0)	(428.0)
	R-HSD [4]	0.986	142	1	6.35
		(1.000)	(92)	(0)	(6.60)
	FCN-HoD [5]	0	0	0	124.18
		(-)	(-)	(-)	(-)
	Ours (Res18)	<u>0.972</u>	<u>146</u>	<u>2</u>	3.32
Ours (Res34)	0.944	170	4	3.36	
Ours (Res50)	0.958	203	3	3.58	
Average	BBL-HoD [3]	(0.876)	(274)	(45.3)	(251)
	R-HSD [4]	0.757	184	23.33	4.17
		(0.968)	(61.6)	(26.0)	(6.50)
	FCN-HoD [5]	0.020	7.33	613.67	74.17
		(-)	(-)	(-)	(-)
	Ours (Res18)	0.974	130	18.0	2.02
Ours (Res34)	<u>0.963</u>	<u>101</u>	<u>14.6</u>	<u>2.06</u>	
Ours (Res50)	0.960	138	12.0	2.16	

C. Evaluation Metrics

The performance of each hotspot detector is evaluated based on several metrics: the recall value (*aka* true-positive-rate, TPR), the number of false alarms (#FA), the number of false negative samples (#FN), and runtime cost (**Time**). These metrics have been widely used in the literature [5]. Additionally, the model performances are visualized through the TPR-to-FA (true-positive-rate to false-alarm) curve, which can be regarded as an ROC (receiver operating characteristic) curve but with an unnormalized horizontal axis. While an ROC curve plots the TPR against the false positive rate (FPR), which is commonly used to assess the performances of binary classifiers, determining the FPR in layout hotspot detection is challenging. This is because an infinite number of non-hotspot regions can be cropped from a layout, resulting in an ill-defined total false alarm count. Therefore, we replace the FPR with the false alarm count to plot the TPR-to-FA curve. Moreover, this still allows for the calculation of the AUROC (area under the ROC curve) value, as the ratio of the area under the TPR-to-FA curve to the total area remains unchanged.

D. Performance Evaluation on ICCAD16

We compare the performance of our LithoHoD against existing state-of-the-art methods on **ICCAD16**. Since the

TABLE V

PERFORMANCE COMPARISON ON **ICCAD-16**. IN (A), THE RIGHT HALF OF EACH **ICCAD-16** SAMPLE IS USED TO CROP THE TRAINING PATCHES, AND THE LEFT HALF IS USED AS THE TESTING SET. IN (B), THE MIDDLE HORIZONTAL STRIP OF EACH SAMPLE IS USED FOR TRAINING, AND THE BOTTOM STRIP IS USED FOR TESTING.

	Datasets	Method	Recall	#FA	#FN	AP
(A)	ICCAD16 Case-2	R-HSD [4]	0.171	263	58	0.010
		FCN-HoD [5]	0.003	26	1011	0.001
		Ours (Res18)	0.844	37	158	0.706
		Ours (Res34)	0.742	42	262	0.566
		Ours (Res50)	0.514	9	493	0.491
	ICCAD16 Case-3	R-HSD [4]	0.971	176	74	0.179
		FCN-HoD [5]	0.000	0	34684	0.000
		Ours (Res18)	0.990	41	362	0.928
		Ours (Res34)	0.987	44	444	0.941
		Ours (Res50)	0.928	35	418	0.930
	ICCAD16 Case-4	R-HSD [4]	0.123	48	64	0.408
		FCN-HoD [5]	0.280	124	306	0.140
Ours (Res18)		0.391	37	259	0.359	
Ours (Res34)		0.459	32	230	0.706	
Ours (Res50)		0.435	35	240	0.409	
(B)	ICCAD16 Case-2	R-HSD [4]	0.863	252	7	0.329
		FCN-HoD [5]	0.078	19	188	0.043
		Ours (Res18)	0.882	19	24	0.798
		Ours (Res34)	0.804	25	40	0.698
		Ours (Res50)	0.726	7	56	0.693
	ICCAD16 Case-3	R-HSD [4]	0.977	102	32	0.373
		FCN-HoD [5]	0.001	20	5235	0.000
		Ours (Res18)	0.797	22	1062	0.797
		Ours (Res34)	0.780	16	1152	0.779
		Ours (Res50)	0.792	10	1008	0.791
	ICCAD16 Case-4	R-HSD [4]	0.904	363	7	0.191
		FCN-HoD [5]	0.969	16	1	0.838
Ours (Res18)		0.781	7	7	0.673	
Ours (Res34)		0.781	15	7	0.501	
Ours (Res50)		0.781	5	7	0.698	

object detection backbone of LithoHoD is a RetinaNet, whose feature extraction backbone can be readily replaced with any network in the ResNet family [27], we evaluate the performance of LithoHoD with different feature extraction backbones, including ResNet-18, ResNet-34, and ResNet-50. Note that in Table IV, the performance values in parentheses are those reported in the BBL-HoD [3], FCN-HoD [5], and R-HSD [4], while the others are obtained from our experimental results. Also, as FCN-HoD and BBL-HoD do not release their official source codes, the performances with FCN-HoD are measured based on our own implementation.

First of all, Table IV shows that LithoHoD consistently outperforms the compared methods. This is attributed to LithoHoD's capability to pinpoint regions at risk of developing hotspots, guided by the pretrained LithoNet integrated into its framework. Additionally, the numbers of false negatives (#FN) associated with LithoHoD variants are, on average, lower than those of other SOTA methods. This fact underscores the importance of incorporating a lithography simulator into the layout hotspot detection framework.

Next, Table V(A) shows the experiments using the right half image for training and the left half for testing, and Table V(B) shows the experiments using the middle strip for training and the bottom strip for testing. To better assess each model's robustness against data variations, we measure the average precision (AP) values denoting the area under the recall-precision curve in Table V. A higher AP value indicates

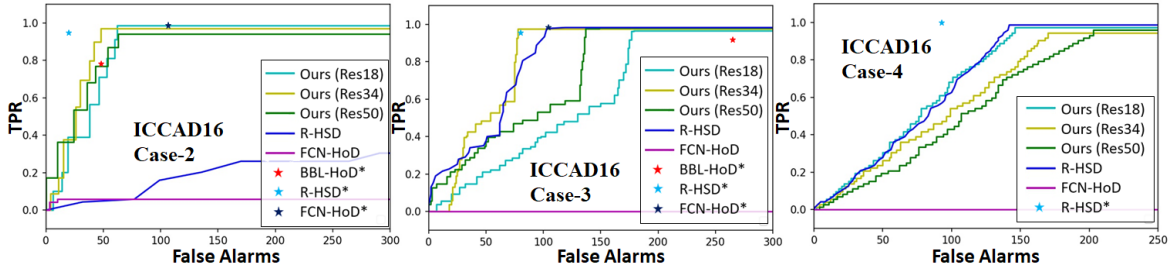


Fig. 6. Performance comparisons in terms of TPR-to-FA curves on ICCAD16 dataset. Left: Case-2; Middle: Case-3; Right: Case-4. In the figure legend, we abbreviate our LithoHoD equipped with different feature extraction backbones as Ours(Res18), Ours(Res34), and Ours(Res50). Note that BBL-HoD*, R-HSD*, and FCN-HoD* are single-point performance values reported in their papers.

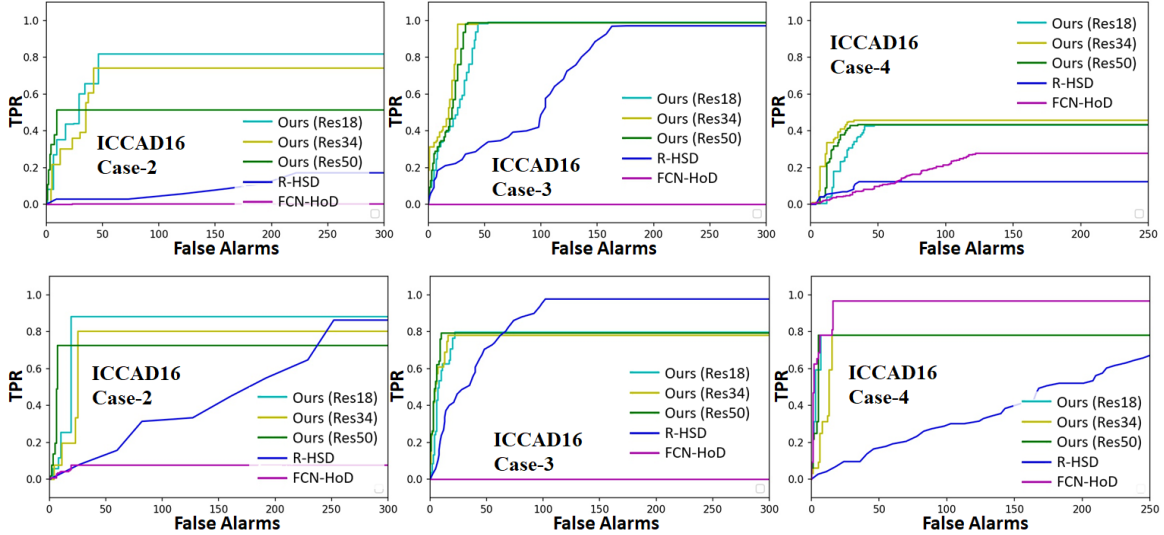


Fig. 7. TPR-to-FA curves of two experiment sets on ICCAD16 dataset. From top to bottom: i) TPR-to-FA curves of the experiment set shown in Table V(A), and ii) TPR-to-FA curves of the experiment set shown in Table V(B).

a better model capability of identifying true positives while preventing false negatives. The two experiments in Table V show that LithoHoD outperforms the two compared SOTAs in AP in most cases, suggesting that LithoHoD can learn from and be deployed on different datasets stably.

Furthermore, experiments with our LithoHoD reveal that various feature extraction backbones are better suited to specific datasets. A deeper backbone generally leads to overfitting when the dataset is less comprehensive, as observed from **ICCAD16** Case-2. As a result, we find that LithoHoD with the ResNet-18 backbone, on average, outperforms the other variants in this case. Additionally, Tables IV and V show that LithoHoD with the ResNet-34 backbone achieves the most consistent performance across all metrics. Hence, we opt for this variant of LithoHoD for the ablation study and for conducting additional experiments on the real-world **UMC20K**. Finally, Fig. 6 and Fig. 7 demonstrate the TPR-to-FalseAlarm curves of different methods on **ICCAD16**, further showing the superiority of LithoHoD on this open dataset.

E. Performance Evaluation on UMC20K

We also conduct a comprehensive performance evaluation on **UMC20K**, a dataset comprising a rich number of real-world layout samples. The results depicted in Fig. 8 and

Table VI unequivocally demonstrate that LithoHoD, guided by the pretrained LithoNet, achieves the highest recall score when employing the ResNet-18 backbone. Furthermore, LithoHoD effectively mitigates the false alarm counts, thanks to LithoNet pre-trained on real-world layout-SEM sample pairs. These findings confirm that leveraging a lithography simulator pre-trained on data collected from a similar domain can substantially enhance the efficacy of a layout hotspot detector. Note that, since the official codes for the R-HSD method [4] and the FCN-HoD method [5] have not been released, all the performance values in Table VI and the curves in Fig. 8 are obtained from our own implementations.

Furthermore, our LithoHoD consistently outperforms previous state-of-the-art methods under the guidance of the lithography simulator, regardless of the type of feature extractor (*e.g.*, ResNet) used. However, the experimental results suggest that LithoHoD with shallower feature extractors (*e.g.* ResNet-18) generally outperforms its counterparts with deeper feature extractors on **UMC-20K**. We attribute this to the fact that IC layout designs typically consist of binary polygons, involving primarily straight lines and rectangles in black-and-white format. Therefore, employing a shallower and simpler feature extractor with fewer parameters often yields superior results. In contrast, deeper feature extraction networks performing

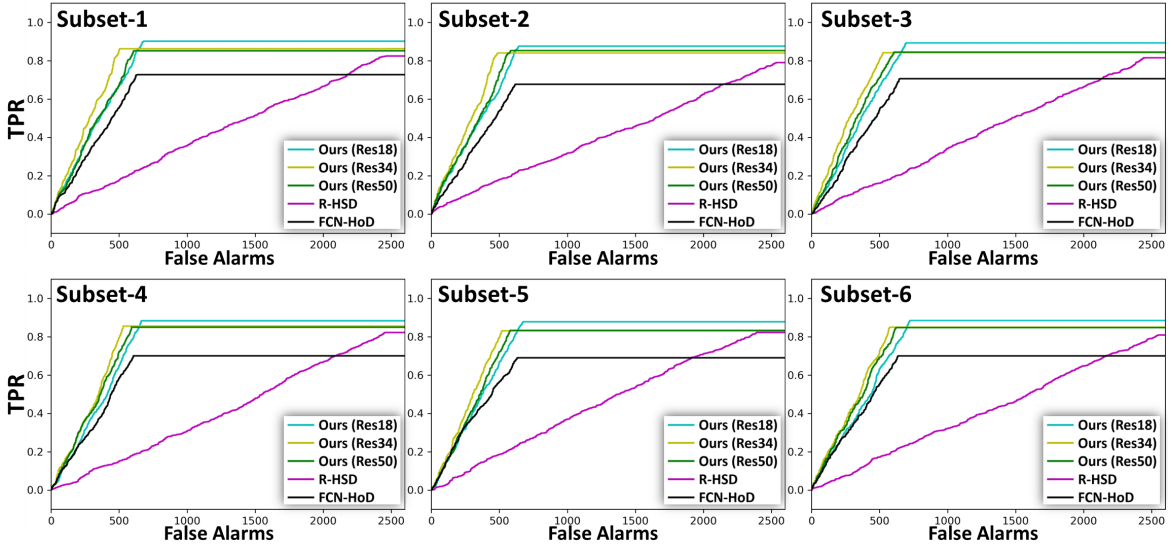


Fig. 8. Comparison of TPR-to-FalseAlarm performances with various hotspot detection models on **UMC20K**. In the figure legend, we abbreviate the LithoHoD equipped with different feature extraction backbones as Ours (Res18), Ours (Res34), and Ours (Res50).

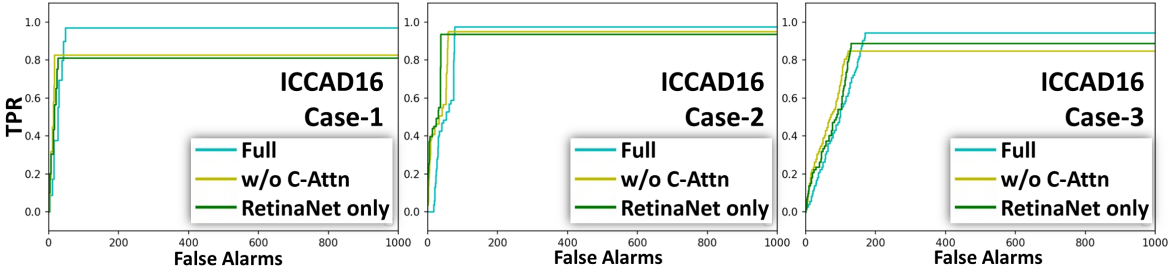


Fig. 9. Ablation Study of LithoHoD on **ICCAD16** in terms of Recall to False-alarm curves. Left: Case-2, Middle: Case-3, Right: Case-4.

well on complex natural images (*e.g.*, street scenes, remote sensing, and product recognition) are less effective in the context of layout hotspot detection. Consequently, this enables our LithoHoD equipped with ResNet-18 to achieve better and more stable hotspot detection results on real-world data.

Experiments on **ICCAD16** and **UMC20K** demonstrate the efficacy of LithoHoD in two distinct scenarios. The first scenario, corresponding to experiments on **UMC20K**, is that the lithography conditions used for hotspot detection are consistent with the lithography conditions of LithoNet’s training dataset. The experiments on **UMC20K** show that when the lithography conditions are the same or similar, the deformation map predicted by LithoNet aids the hotspot detector well, leading to superior detection performance.

On the other hand, corresponding to experiments on **ICCAD16**, the second scenario is that there exists a significant domain gap between the lithography conditions for the pre-trained LithoNet and the hotspot detector. In this scenario, the deformation map predicted by LithoNet will be less accurate. However, even with inconsistent lithography conditions, LithoNet can still predict “relative” local deformations caused by different layout patterns. With the supervision of the hotspot labels, these local deformation features can be properly scaled and weighted through the self- and cross-attention mechanisms of the CMF module. In this way, LithoHoD can tolerate

the inaccuracies of deformation features to some extent by learning to select useful deformation features during feature fusion via its self- and cross-attention mechanisms. This is evidenced by the ablation study on **ICCAD16** (see Table VII), where LithoNet was pre-trained on the UMC dataset.

In the worst-case scenario, where the domain gap in lithography conditions is so large that LithoNet becomes ineffective, LithoHoD will revert to functioning as a traditional hotspot detector. In this situation, its attention mechanisms will discard LithoNet’s deformation features.

In summary, the experimental results support that our LithoHoD is effective even without fine-tuning its lithography simulator. It can still learn the relationship between the deformation maps, layouts, and hotspot ground truths through the training routine, thereby improving hotspot detection performance, as evidenced by the results on **ICCAD16**. Nevertheless, if LithoNet can be fine-tuned based on the current lithography conditions to bridge the domain gap, the performance gain with LithoHoD will be significant, as demonstrated by the results on **UMC20K**.

F. Ablation Studies

We conduct two ablation studies to validate the individual contributions of LithoHoD’s modules to the performance of LithoHoD on **ICCAD16** and **UMC20K**, respectively. Fig. 9

TABLE VI
PERFORMANCE COMPARISON OF LITHOHOD WITH VARIOUS FEATURE
EXTRACTION BACKBONES AND TWO SOTA METHODS ON **UMC20K**'S
TESTING SUBSETS

Datasets	Method	Recall	#FA	#FN	Time (s)
Subset-1 481 Images 1284 Hotspots	R-HSD [4]	0.824	2467	226	78.44
	FCN-HoD [5]	0.727	673	351	16.01
	Ours (Res18)	0.901	683	127	32.43
Subset-2 481 Images 1416 Hotspots	Ours (Res34)	0.862	507	177	32.76
	Ours (Res50)	0.851	612	191	33.13
	R-HSD [4]	0.790	2545	298	80.42
Subset-3 481 Images 1318 Hotspots	FCN-HoD [5]	0.678	619	458	15.44
	Ours (Res18)	0.876	646	176	33.83
	Ours (Res34)	0.840	488	227	32.83
Subset-4 481 Images 1339 Hotspots	Ours (Res50)	0.852	584	209	33.46
	R-HSD [4]	0.815	2453	224	78.84
	FCN-HoD [5]	0.706	650	388	15.38
Subset-5 481 Images 1276 Hotspots	Ours (Res18)	0.892	695	142	33.32
	Ours (Res34)	0.841	526	209	33.51
	Ours (Res50)	0.845	607	205	33.09
Subset-6 482 Images 1378 Hotspots	R-HSD [4]	0.822	2453	239	79.05
	FCN-HoD [5]	0.700	604	402	15.30
	Ours (Res18)	0.883	663	157	33.35
Average	Ours (Res34)	0.855	530	194	33.33
	Ours (Res50)	0.849	591	202	33.04
	R-HSD [4]	0.822	2397	227	78.94
Total 8011 Hotspots	FCN-HoD [5]	0.699	632	396	15.23
	Ours (Res18)	0.878	675	156	32.35
	Ours (Res34)	0.831	519	216	32.89
Subset-6 482 Images 1378 Hotspots	Ours (Res50)	0.832	580	214	33.09
	R-HSD [4]	0.808	2550	264	78.64
	FCN-HoD [5]	0.700	636	414	15.41
Average	Ours (Res18)	0.844	726	160	34.52
	Ours (Res34)	0.849	578	208	33.09
	Ours (Res50)	0.847	625	211	33.49
Total 8011 Hotspots	R-HSD [4]	0.813	2478	246	79.06
	FCN-HoD [5]	0.701	630	402	15.46
	Ours (Res18)	0.889	681	153	33.33
Average	Ours (Res34)	0.846	525	205	33.06
	Ours (Res50)	0.846	600	205	33.22

TABLE VII
ABLATION STUDY OF THE MODULES OF LITHOHOD ON **ICCAD16**,
WHERE THE BEST AUC SCORES ARE HIGHLIGHTED IN BOLD

Benchmark	Method	Recall	#FA	AUC score
ICCAD16 Case-2	(a) RetinaNet only	0.812	25	0.800
	(b) w/o C-Attn	0.826	17	0.818
	(c) Full Model	0.971	55	0.946
ICCAD16 Case-3	(a) RetinaNet only	0.958	60	0.916
	(b) w/o C-Attn	0.949	60	0.921
	(c) Full Model	0.974	78	0.925
ICCAD16 Case-4	(a) RetinaNet only	0.903	130	0.827
	(b) w/o C-Attn	0.847	121	0.798
	(c) Full Model	0.944	170	0.860

and Table VII present the results of the ablation study on **ICCAD16**. This ablation study verifies how individual modules contribute to LithoHoD by individually removing the two modules: i) the lithography simulator and ii) the channel-attention module within the object detection backbone. We use the term ‘‘RetinaNet only’’ to denote the first scenario in which the pretrained LithoNet is removed by deactivating the cross-model feature fusion (CMF) module. Second, ‘‘w/o C-Attn’’ indicates the removal of the channel-wise attention module in between ResNet and FPN, *i.e.*, the C-Attn module shown in Fig. 2, implying the use of an unmodified RetinaNet backbone.

Table VII demonstrates a significant drop in recall and AUC

TABLE VIII
ABLATION STUDY ON THE MODULES OF LITHOHOD (WITH RES34
BACKBONE) ON **UMC20K**, WHERE THE BEST RESULTS ARE HIGHLIGHTED
IN BOLD

Benchmark	Method	Recall	#FA	AUC
Subset-1 481 Images 1284 Hotspots	(a) RetinaNet only	0.693	222	0.621
	(b) w/o C-Attn	0.921	985	0.504
	(c) Full Model	0.862	507	0.656
Subset-2 481 Images 1416 Hotspots	(a) RetinaNet only	0.652	183	0.539
	(b) w/o C-Attn	0.899	1036	0.450
	(c) Full Model	0.840	488	0.644
Subset-3 481 Images 1318 Hotspots	(a) RetinaNet only	0.687	217	0.620
	(b) w/o C-Attn	0.915	1019	0.449
	(c) Full Model	0.841	526	0.644
Subset-4 481 Images 1339 Hotspots	(a) RetinaNet only	0.701	227	0.621
	(b) w/o C-Attn	0.908	1019	0.449
	(c) Full Model	0.855	530	0.625
Subset-5 481 Images 1276 Hotspots	(a) RetinaNet only	0.677	229	0.604
	(b) w/o C-Attn	0.909	1043	0.466
	(c) Full Model	0.831	519	0.625
Subset-6 482 Images 1378 Hotspots	(a) RetinaNet only	0.668	229	0.598
	(b) w/o C-Attn	0.895	1049	0.447
	(c) Full Model	0.849	578	0.615

scores when deactivating any of these modules. Because the results in Table VII are obtained with the models trained on **ICCAD16**, the increase in false alarms can be attributed to two factors. The first factor is the similarities among patterns in **ICCAD16**'s three cases. The second is that, by leveraging the lithography simulator, LithoHoD can detect those areas in **ICCAD16** that are not labeled as hotspots but have the potential to develop hotspots, thereby potentially leading to more false alarms.

Table VIII and Fig. 10 show the ablation study results on **UMC-20K**, demonstrating the individual contributions of LithoHoD's modules on real-world hotspot detection cases. Similar to the findings reported in Table VII, the removal of individual modules leads to an AUC performance drop, highlighting the indispensability of each module in enhancing the model performance. Besides, while the full model equipped with a lithography simulator tends to generate a higher number of false alarms (#FA) compared to the object detector alone (*i.e.*, ‘‘RetinaNet only’’), the superior recall and AUC scores of our full model still suggest that a lithography simulator can facilitate hotspot detection. This demonstrates providing the object detector with a predicted lithography deformation map effectively aids in identifying potential hotspot areas in real-world cases. Furthermore, the results in ‘‘w/o C-Attn’’ demonstrate a significant increase in false alarms and low AUC scores with illusory high recall values when the channel-attention module is removed. This suggests that the channel-attention module in our object detection backbone effectively reduces false alarms, albeit slightly decreasing the recall value, thus contributing to an optimized full model in terms of AUC.

The above ablation studies reveal that integrating the lithography deformation features with the layout shape features can more effectively identify layout hotspot areas, including potentially risky regions, in real-world scenarios.

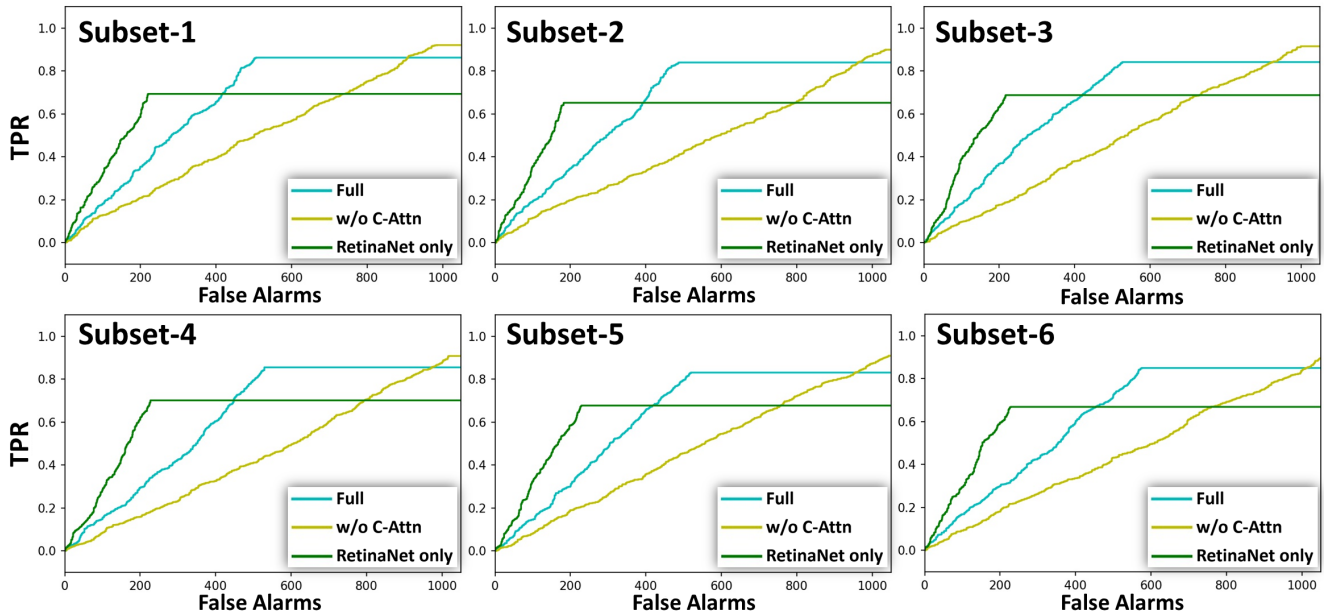


Fig. 10. Ablation Study of LithoHoD on UMC20 in terms of Recall to False-alarm curves.

V. CONCLUSION

In this work, we proposed a lithography simulator-guided hotspot detection framework, namely LithoHoD, capable of integrating lithography deformation features with the object detection features of a given layout. The proposed LithoHoD mainly consists of two modules: a shape feature extractor (RetinaNet) and a lithography simulator (LithoNet). Additionally, we introduced a cross-domain attention mechanism to fuse the shape features from RetinaNet with the local lithography deformation features from LithoNet. Our experimental results confirm that the incorporation of a lithographic simulator significantly enhances the adaptability of a conventional object detection model for layout hotspot detection tasks. Notably, our LithoHoD demonstrates superior performances on both the simulated ICCAD16 dataset and a real-world UMC20K dataset provided by an IC-fab foundry. While this simulator-guided framework may entail a slightly higher computational time complexity than previous state-of-the-art methods, its recall value and AUC score outperform these methods, setting a new benchmark in hotspot detection for IC fabrication. This work demonstrates the successful repurposing of object detectors for hotspot detection tasks with appropriately learned features, thereby laying a foundation for the future development of more advanced hotspot detection models.

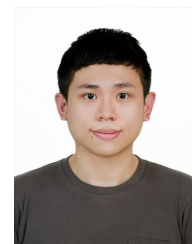
REFERENCES

- [1] Y. Jiang, F. Yang, B. Yu, D. Zhou, and X. Zeng, "Efficient layout hotspot detection via binarized residual neural network ensemble," *IEEE Trans. Comput.-Aided Design Integr. Circuits Syst.*, vol. 40, no. 7, pp. 1476–1488, July 2021.
- [2] H. Geng, H. Yang, L. Zhang, J. Miao, F. Yang, X. Zeng, and B. Yu, "Hotspot detection via attention-based deep layout metric learning," in *Proc. IEEE/ACM Int. Conf. Comput.-Aided Design*, Nov. 2020, pp. 1–8.
- [3] H. Yang, J. Su, Y. Zou, Y. Ma, B. Yu, and E. Young, "Layout hotspot detection with feature tensor generation and deep biased learning," *IEEE Trans. Comput.-Aided Des. Integr. Circuits Syst.*, vol. 38, no. 6, pp. 1175–1187, 2019.
- [4] R. Chen, W. Zhong, H. Yang, H. Geng, Y. Fan, X. Zeng, and B. Yu, "Faster region-based hotspot detection," *IEEE Trans. Comput.-Aided Des. Integr. Circuits Syst.*, vol. 41, no. 3, pp. 669–680, 2022.
- [5] T. Gai, T. Qu, S. Wang, X. Su, R. Xu, Y. Wang, J. Xue, Y. Su, Y. Wei, and T. Ye, "Flexible hotspot detection based on fully convolutional network with transfer learning," *IEEE Trans. Comput.-Aided Des. Integr. Circuits Syst.*, vol. 41, no. 11, pp. 4626–4638, 2021.
- [6] B. Zhu, R. Chen, X. Zhang, F. Yang, X. Zeng, B. Yu, and M. Wong, "Hotspot detection via multi-task learning and transformer encoder," in *Proc. IEEE/ACM Int. Conf. Comput.-Aided Design*, Nov. 2021, pp. 1–8.
- [7] H.-C. Shao, C.-W. Lin, and S.-Y. Fang, "Data-driven approaches for process simulation and optical proximity correction," in *Proc. Asia Southern Pacific Design Autom. Conf.*, Jan. 2023, pp. 1–6.
- [8] S. Ren, K. He, R. Girshick, and J. Sun, "Faster R-CNN: Towards real-time object detection with region proposal networks," *Proc. Adv. Neural Inform. Process. Syst.*, vol. 28, Jan. 2015.
- [9] Y.-T. Yu, G.-H. Lin, I. Jiang, and C. Chiang, "Machine-learning-based hotspot detection using topological classification and critical feature extraction," in *Proc. Design Autom. Conf.*, June 2013, pp. 1–6.
- [10] T. Matsunawa, J.-R. Gao, B. Yu, and D. Pan, "A new lithography hotspot detection framework based on adaboost classifier and simplified feature extraction," in *Design-Process-Technology Co-optimization for Manufacturability IX*, vol. 9427, 2015, pp. 201–211.
- [11] X. Lin, J. Pan, J. Xu, Y. Chen, and C. Zhuo, "Lithography hotspot detection via heterogeneous federated learning with local adaptation," in *Proc. IEEE Asian South Pacific Design Autom. Conf.*, Jan. 2022, pp. 166–171.
- [12] R. Girshick, J. Donahue, T. Darrell, and J. Malik, "Rich feature hierarchies for accurate object detection and semantic segmentation," in *Proc. IEEE/CVF Conf. Comput. Vis. Pattern Recog.*, June 2014, pp. 580–587.
- [13] R. Girshick, "Fast r-cnn," in *Proc. Int. Conf. Comput. Vis.*, Oct. 2015, pp. 1440–1448.
- [14] J. Redmon, S. Divvala, R. Girshick, and A. Farhadi, "You only look once: Unified, real-time object detection," in *Proc. IEEE/CVF Conf. Comput. Vis. Pattern Recog.*, June 2016, pp. 779–788.
- [15] J. Redmon and A. Farhadi, "YOLO9000: better, faster, stronger," in *Proc. IEEE/CVF Conf. Comput. Vis. Pattern Recog.*, June 2017, pp. 7263–7271.
- [16] —, "YOLOv3: An incremental improvement," *arXiv preprint arXiv:1804.02767*, 2018.
- [17] A. Bochkovskiy, C.-Y. Wang, and H.-Y. M. Liao, "YOLOv4: Optimal speed and accuracy of object detection," *arXiv preprint arXiv:2004.10934*, 2020.
- [18] W. Liu, D. Anguelov, D. Erhan, C. Szegedy, S. Reed, C.-Y. Fu, and

- A. Berg, "Ssd: Single shot multibox detector," in *Proc. European Conf. Comput. Vis.*, Oct. 2016, pp. 21–37.
- [19] T.-Y. Lin, P. Goyal, R. Girshick, K. He, and P. Dollár, "Focal loss for dense object detection," in *Proc. Int. Conf. Comput. Vis.*, Oct. 2017, pp. 2980–2988.
- [20] T.-Y. Lin, P. Dollár, R. Girshick, K. He, B. Hariharan, and S. Belongie, "Feature pyramid networks for object detection," in *Proc. IEEE/CVF Conf. Comput. Vis. Pattern Recognit.*, June 2017, pp. 2117–2125.
- [21] Y. Watanabe, T. Kimura, T. Matsunawa, and S. Nojima, "Accurate lithography simulation model based on convolutional neural networks," in *Optical Microlithography XXX*, vol. 10147, 2017.
- [22] H. Yang, S. Li, Y. Ma, B. Yu, and E. F. Young, "GAN-OPC: Mask optimization with lithography-guided generative adversarial nets," in *Proc. ACM/ESDA/IEEE Design Autom. Conf.*, 2018, pp. 1–6.
- [23] W. Ye, M. B. Alawieh, Y. Lin, and D. Z. Pan, "LithoGAN: End-to-end lithography modeling with generative adversarial networks," in *ACM/IEEE Design Autom. Conf.*, 2019, pp. 107:1–107:6.
- [24] H.-C. Shao, C.-Y. Peng, J.-R. Wu, C.-W. Lin, S.-Y. Fang, P.-Y. Tsai, and Y.-H. Liu, "From IC layout to die photograph: A CNN-based data-driven approach," *IEEE Trans. Comput.-Aided Design Integr. Circuits Syst.*, vol. 40, no. 5, pp. 957–970, May 2021.
- [25] H.-C. Shao, H.-L. Ping, K.-S. Chen, W.-T. Su, C.-W. Lin, S.-Y. Fang, P.-Y. Tsai, and Y.-H. Liu, "Keeping deep lithography simulators updated: Global-local shape-based novelty detection and active learning," *IEEE Trans. Comput.-Aided Design Integr. Circuits Syst.*, vol. 42, no. 3, pp. 1010–1014, Mar. 2023.
- [26] Y.-T. Yu, Y.-C. Chan, S. Sinha, I. Jiang, and C. Chiang, "Accurate process-hotspot detection using critical design rule extraction," in *Proc. Design Autom. Conf.*, June 2012, pp. 1167–1172.
- [27] K. He, X. Zhang, S. Ren, and J. Sun, "Deep residual learning for image recognition," in *Proc. IEEE/CVF Conf. Comput. Vis. Pattern Recognit.*, 2016, pp. 770–778.
- [28] S. Woo, J. Park, J.-Y. Lee, and I. Kweon, "CBAM: Convolutional block attention module," in *Proc. European Conf. Comput. Vis.*, Oct. 2018, pp. 3–19.
- [29] H. Zhang, I. Goodfellow, D. Metaxas, and A. Odena, "Self-attention generative adversarial networks," in *Proc. Int. Conf. Mach. Learn.*, 2019, pp. 7354–7363.
- [30] Z. Zheng, P. Wang, W. Liu, J. Li, R. Ye, and D. Ren, "Distance-IoU loss: Faster and better learning for bounding box regression," in *Proc. AAAI Conf. Artif. Intell.*, vol. 34, no. 07, Jan. 2020, pp. 12 993–13 000.
- [31] R. Topaloglu, "ICCAD-2016 CAD contest in pattern classification for integrated circuit design space analysis and benchmark suite," in *Proc. IEEE/ACM Int. Conf. Comput.-Aided Design*, Nov. 2016, pp. 1–4.



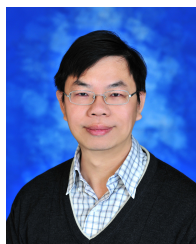
Hao-Chiang Shao (Member, IEEE) received his Ph.D. degree in electrical engineering from National Tsing Hua University, Taiwan, in 2012. He has been an Assistant Professor with the Inst. Data Science and Information Computing, National Chung Hsing University, Taiwan, since 2022. During 2018 to 2022, he was an Assistant Professor with the Dept. Statistics and Information Science, Fu Jen Catholic University, Taiwan. In 2017–2018, he was an R&D engineer with the Computational Intelligence Technology Center, Industrial Technology Research Institute, Taiwan, taking charges of DNN-based automated optical inspection projects; during 2012 to 2017, he was a postdoctoral researcher with the Institute of Information Science, Academia Sinica, involved in *Drosophila* brain research projects. His research interests include 2D+Z image atlas and 3D mesh processing, big image data analysis, classification methods, deep learning and computer vision, and image forgery detection techniques.



Guan-Yu Chen received his B.S. degree in Electronic Engineering from National Central University in 2020 and M.S. degree in Electrical Engineering from National Tsing Hua University in 2023. He joined Novatek Microelectronics Corp., Hsinchu, Taiwan, as a software/firmware engineer in 2023. His research interests lie in computer vision, machine learning, and visual analytics for IC design for manufacturability.



Yu-Hsien Lin received the B.S. degree in computer science from the Fu Jen Catholic University, New Taipei City, Taiwan, in 2020, Taiwan, the M.A. degree in applied statistics from Fu Jen Catholic University, in 2022. He is currently pursuing his Ph.D. degree at the Department of Electrical Engineering of National Tsing Hua University, Hsinchu, Taiwan. His research interests mainly lie in machine learning, electronic design automation, and computer vision.



Chia-Wen Lin (Fellow, IEEE) received his Ph.D. degree from National Tsing Hua University (NTHU), Hsinchu, Taiwan, in 2000. Dr. Lin is currently a Distinguished Professor with the Department of Electrical Engineering and the Institute of Communications Engineering, NTHU. His research interests include image/video processing and computer vision. He has served as a Fellow Evaluation Committee member (2021–2023), BoG Members-at-Large (2022–2024), and Distinguished Lecturer (2018–2019) of IEEE CASS. He was Chair of IEEE ICME Steering Committee (2020–2021). He served as TPC Co-Chair of IEEE ICIP 2019 and IEEE ICME 2010, and General Co-Chair of IEEE VCIP 2018. He received two best paper awards from VCIP 2010 and 2015. He was an Associate Editor of IEEE TRANSACTIONS ON IMAGE PROCESSING, IEEE TRANSACTIONS ON CIRCUITS AND SYSTEMS FOR VIDEO TECHNOLOGY, IEEE TRANSACTIONS ON MULTIMEDIA, and IEEE MULTIMEDIA.



Shao-Yun Fang (Member, IEEE) received a B.S. degree in electrical engineering from the National Taiwan University (NTU), Taipei, Taiwan, in 2008 and a Ph.D. degree from the Graduate Institute of Electronics Engineering, NTU, in 2013. She is currently a Professor of the Department of Electrical Engineering, National Taiwan University of Science and Technology, Taipei, Taiwan. Her research interests focus on physical design and design for manufacturability for integrated circuits. Dr. Fang received two Best Paper Awards from the 2016 International Conference on Computer Design and the 2016 International Symposium on VLSI Design, Automation, and Test, and two Best Paper Nominations from International Symposium on Physical Design in 2012 and 2013.



manufacturing yield.

Pin-Yian Tsai received his M.S. degree in Physics from National Tsing Hua University (NTHU), Taiwan, in 2008. He is currently a technical manager of the Product Engineering Department in United Microelectronics Corporation (UMC). He led the launch of UMC's first 14nm product tape out (2017) and is currently working and researching on the field of Design for Manufacturing (DFM). He is now focusing on developing methods for predicting weak patterns in layout manufacturing and automatic optical proximity correction (OPC) to improve the



Yan-Hsiu Liu received his M.S. degree in Chemistry from National Tsing Hua University (NTHU), Taiwan, in 2002. In 2004, he joined United Microelectronics Corporation (UMC) as a process integration engineer in Hsinchu, Taiwan. He is currently working as a deputy department manager on the development of smart manufacturing and responsible for industry-academia cooperation/collaboration. His research interests include the areas of intelligent manufacturing systems, adaptive parameter estimation, and neural networks.